POLITECNICO DI TORINO
Repository ISTITUZIONALE

Dissolution behavior and bioactivity of lithium-doped 45S5 bioglass: An experimental and molecular dynamics simulation study

Original
Dissolution behavior and bioactivity of lithium-doped 45S5 bioglass: An experimental and molecular dynamics simulation study / Moghanian, A., Baino, F.. - In: NEXT MATERIALS. - ISSN 2949-8228. - ELETTRONICO. - 13:(2026), pp. 1-11. [10.1016/j.nxmate.2026.103409]

Availability:
This version is available at: 11583/3017061 since: 2026-10-27T12:51:01Z

Publisher:
Elsevier

Published
DOI:10.1016/j.nxmate.2026.103409

Terms of use:

This article is made available under terms and conditions as specified in the corresponding bibliographic description in the repository

Publisher copyright

(Article begins on next page)

20 November 2026

Next Materials 13 (2026) 103409

Contents lists available at ScienceDirect

Next Materials

journal homepage: www.sciencedirect.com/journal/next-materials

Research article

Dissolution behavior and bioactivity of lithium-doped 45S5 bioglass: An experimental and molecular dynamics simulation study

Amirhossein Moghanian [a,*], Francesco Baino [b,*]

[a] Department of Materials Engineering, Faculty of Engineering, Imam Khomeini International University, Qazvin 34149-16818, Iran
[b] Institute of Materials Physics and Engineering, Department of Applied Science and Technology, Politecnico di Torino, Torino, Italy

ARTICLE INFO

Keywords:
Bioactive glass
Lithium
Molecular dynamics
Dissolution
Atomic-scale structure

ABSTRACT

This study used molecular dynamics (MD) simulations and experimental analyses to evaluate lithium (Li)-doped 45S5 bioglass (45-L) for tissue engineering (TE) applications. Li_2O was substituted for Na_2O in the 45S5 bioglass composition with 0–20 mol%, then resulting in new materials labeled as 45-L0 to 45-L20. Atomic-scale characteristics were evaluated in terms of short- and medium-range structure. Short-range structure presented pair distribution function (PDF) and coordination number (CN) of the samples showing that the Li–O bonds were shorter in the structure due to the smaller ionic radius, and the CN was calculated to be 4.03. Additionally, the medium-range structure of the Li-doped BGs showed dominant non-bridging oxygens (NBOs) with negligible P–O–P bonds, while Li_2O did not change the bond types significantly. Additionally, Q^n analysis showed that the Li incorporation promoted the formation of Q^3 species and increased network connectivity (NC) from 1.92 for 45-L0 to 1.96 for 45-L20. Moreover, Li_2O enhanced structural density but was expected to reduce the dissolution of BGs. ICP-AES analysis showed that the release of Si^{4+} ions decreased with higher Li_2O content. Meanwhile, SEM images showed a bioactive behavior of the 45-L5 sample while immersed in SBF solution for 14 days. Taken together, the integration of MD simulations, ICP-AES data and SEM showed an interesting balance of properties for moderate Li_2O content, and especially the 45-L5 composition can be considered as a promising candidate for bone tissue regeneration applications.

1. Introduction

For many years, bioceramics have been used for damaged tissue and bone regeneration; however, the field of bioceramics was changed after the invention of 45S5 bioglass in 1969 by Prof. Hench [1] with the chemical composition of 45 wt% SiO_2, 24.5 wt% Na_2O, 24.5 wt% CaO, 6 wt% P_2O_5. This material was the first to be defined as "bioactive" as it could bond with living tissue through a newly-formed surface layer of hydroxyapatite (HA) [2–4]. BGs are a subgroup of bioactive materials that can be utilized in many applications because of their bioactivity, osteoconductive properties, and biodegradability [5,6]. Typically, BGs can be synthesized using either the conventional melt-quench method, which is relatively fast and optimal for mass production, or sol-gel approaches that allow a finer control over composition but are time-consuming [7]. Silicate-based BGs are the main category of BGs due to their ability to conduct surface reactions and ion release, while having the ability to be modified by dopant elements, allowing researchers to design versatile formulations with various compositions suitable for a range of biomedical and therapeutic applications [8–10]. From a general perspective, compositional design by ion doping of glasses and glass-ceramics is very useful to tailor the microstructure and functional properties of such materials, also beyond the biomedical scenario (*e.g.* dielectric properties [11]).

The release of biologically active ions from the BG surface may lead to stimulating osteogenesis, angiogenesis, and antibacterial responses [12–15]. In recent studies, lithium (Li)-doped BGs (L-BGs) have been reported to have potential biomedical applications [16–19]. Simila et al. [20] showed that Li_2O-containing BGs exhibited *in vitro* bioactivity through the formation of an apatite-like Ca-P surface layer after immersion in SBF. Additionally, Wei et al. [21] reported that Li-BG extracts promoted the proliferation of endothelial cells and Schwann cells, which are crucial in nerve regeneration. Cordero et al. [22] utilized Li-doped 45S5 bioglass in the treatment of oral diseases and reported that the alkaline environment produced by the BG elicited antibacterial effects while promoting the recovery of the microhardness of demineralized teeth. Additionally, several studies show the positive effect of Li in

* Corresponding authors.
E-mail addresses: Moghanian@eng.ikiu.ac.ir (A. Moghanian), francesco.baino@polito.it (F. Baino).

https://doi.org/10.1016/j.nxmate.2026.103409
Received 27 April 2026; Received in revised form 4 August 2026; Accepted 31 August 2026
2949-8228/© 2026 The Author(s). Published by Elsevier Ltd. This is an open access article under the CC BY license (http://creativecommons.org/licenses/by/4.0/).

enhancing osteoblast proliferation [23–25].

Experimental assessments are key in evaluating the properties of BGs; however, they are costly and time-consuming, while having the risk of laboratory limitations and synthesis defects. To overcome these limitations, computational materials science has been used by scientists as an efficient alternative method in recent years [26–28]. Molecular dynamics (MD) is one of the most powerful tools in simulating various materials and can effectively predict the properties using potential parameters and force fields to mimic atomic interactions, thus providing structural information of BGs for further use in designing optimal compositions [29–32].

This study aimed to evaluate the effect of Li_2O on the structure of 45S5 bioglass using MD simulations. Li_2O was substituted for Na_2O in the structure at 0–20 mol%. MD simulations yielded an estimation of short-range structural data, like pair distribution function (PDF) and coordination number (CN), as well as medium-range structure data such as oxygen bonds, Q^n distribution, network connectivity (NC), ion clustering, and F_{net}. Finally, experimental analyses were conducted to validate the simulations and find a balanced composition to be utilized in tissue engineering (TE) and biomedical applications.

2. Materials and methods

2.1. Simulation details

All of the L-BG samples in this simulation had a set of partial charge pairwise potentials. For every BG simulation, the potentials' short-range interaction had the Buckingham form (Table 1), and the potentials' long-range interaction had the Coulomb form. Buckingham potential forms have been presented by Eq. (1), where A, ρ, and C are Buckingham potential parameters, and r is the distance between two atoms. Moreover, Table 2 shows the atomic properties of the simulation box and the obtained density of the BGs.

$$V(r) = A\exp\left(-\frac{r}{\rho}\right) - \frac{C}{r^6} \quad (1)$$

The melt–quench procedure was performed using the large-scale atomic/molecular massively parallel simulator (LAMMPS) package [36]. The initial configuration was generated with randomly distributed positions of atoms in the simulation box. The velocity–Verlet algorithm with a 1 fs timestep was employed, and long-range Coulombic interactions were calculated using the Ewald summation method [37]. Temperature and pressure were controlled using Nosé–Hoover thermostats and barostats [38–40]. The protocol followed these steps:

1. Melting stage:

The system was heated to 5000 K under the NVT ensemble and equilibrated for 20 ps to ensure complete melting.

2. High-temperature equilibration:

An additional 150 ps of NVT equilibration at 5000 K was added to eliminate any artificial effects originating from the random initial atomic distribution.

Table 1
Buckingham potential parameters [33–35].

Pairs	A (eV)	ρ (Å)	C (eV/Å^6)
$Si^{+2.4\text{-}O-1.2}$	13,702.905	0.193817	54.681
$Ca^{+1.2\text{-}O-1.2}$	7747.1834	0.252623	93.109
$P^{+3.0\text{-}O-1.2}$	26,655.472	0.181968	86.856
$Na^{+0.6\text{-}O-1.2}$	4383.7555	0.243838	30.70
$Li^{+1.2\text{-}O-1.2}$	14,566.637	0.245015	81.773
$O^{-1.2\text{-}O-1.2}$	2029.2204	0.343645	192.58

3. Cooling stage:

The melt was cooled from 5000 K to 3000 K at a rate of 1 K/ps under the NVT ensemble.

4. Intermediate equilibration:

At 3000 K, the structure was equilibrated for 100 ps under the NPT ensemble to obtain the density of the BG system.

5. Quenching and final equilibration:

The system was then quenched to 300 K under NPT and equilibrated for additional 50 ps at 300 K.

6. Structural analysis stage:

After the equilibration, the simulation was continued for an additional 20 ps under the NVE ensemble at 300 K, with one configuration recorded every 10 fs, yielding 2000 equilibrium configurations per simulation used for temporal averaging of the structural descriptors.

Structural properties were analyzed using the final equilibrated configuration at 300 K. Fig. 1 shows the simulated structure of BGs with different Li_2O content. The weighted average method was used to calculate the average bond length according to this equation: $r_{ave} = \frac{\sum_i r_i g(r_i)}{\sum_i g(r_i)}$. In addition, this was calculated from the distance 0 to the first minimum of the PDF curve after its first peak so that only the average bond length was calculated.

2.2. Experimental details

The L-BG samples were synthesized using the melt-quench approach at 1450 ºC. All the reagents were supplied by Merck KGaA (Germany), specifically silicon dioxide (SiO_2, purity ≥ 99.5%), calcium carbonate ($CaCO_3$, purity ≥ 99.0%), sodium carbonate (Na_2CO_3, purity ≥ 99.5%), diphosphorus pentoxide (P_2O_5, purity ≥ 98.0%), and lithium carbonate (Li_2CO_3, purity ≥ 99.0%). The nominal composition of the 45S5 (in wt %) was 45.0% SiO_2, 24.5% CaO, 24.5% Na_2O, and 6.0% P_2O_5. Lithium was introduced at the expense of Na_2O (both are monovalent cations). Subsequently, the molten glass was quenched, followed by annealing at 500 °C for 30 min to relieve internal stresses, and then was slowly cooled to room temperature at a rate of 5 °C/min. The produced glass samples were ground and passed through a 45 μm sieve to obtain powders with particle size below 45 μm to be used for dissolution testing. Ion concentrations were evaluated using inductively coupled plasma atomic emission spectroscopy (ICP-AES), and the pH values were measured by a calibrated pH meter. For the dissolution test, 0.2 g of glass powder was immersed in 20 mL of SBF in polyethylene containers. To ensure consistency in dissolution measurements, the particle size of the glass powders was kept below 45 μm for all tests, and the surface area-to-volume (Sa/Vs) ratio was fixed at 0.1 cm^{-1}, following the relationship Sa/Vs = 0.1 cm^{-1}. At predetermined time intervals (6, 12, 18, and 24 h), the immersion solution was collected for analysis. The concentrations of Si and Li ions released into the SBF were determined by ICP-AES. Additionally, the pH of the solution was measured at each time point. The dissolution analysis was performed with 3 repetitions, and the values were reported as mean ± standard deviation. Additionally, field emission scanning electron microscopy (FESEM, model: SEM5000, CIQTEK, China) was employed, operated at an accelerating voltage of 1 kV, to observe the formation and morphology of calcium-phosphate phases. Before FESEM observation, the samples were coated with a thin layer of gold to achieve electrical conductivity.

Table 2
Composition and number of atoms adopted in the simulation, along with the resulting density.

BGs	Number of Si atoms	Number of Ca atoms	Number of Li atoms	Number of Na atoms	Number of O atoms	Number of P atoms	Total number of atoms	Density obtained (g/cm^3)
45-L0	461	269	0	488	1565	52	2835	2.673801
45-L1	461	269	20	468	1565	52	2835	2.675595
45-L3	461	269	60	428	1565	52	2835	2.657314
45-L5	461	269	100	388	1565	52	2835	2.654027
45-L8	461	269	160	328	1565	52	2835	2.650549
45-L10	461	269	200	288	1565	52	2835	2.626729
45-L15	461	269	300	188	1565	52	2835	2.608347
45-L20	461	269	400	88	1565	52	2835	2.595322

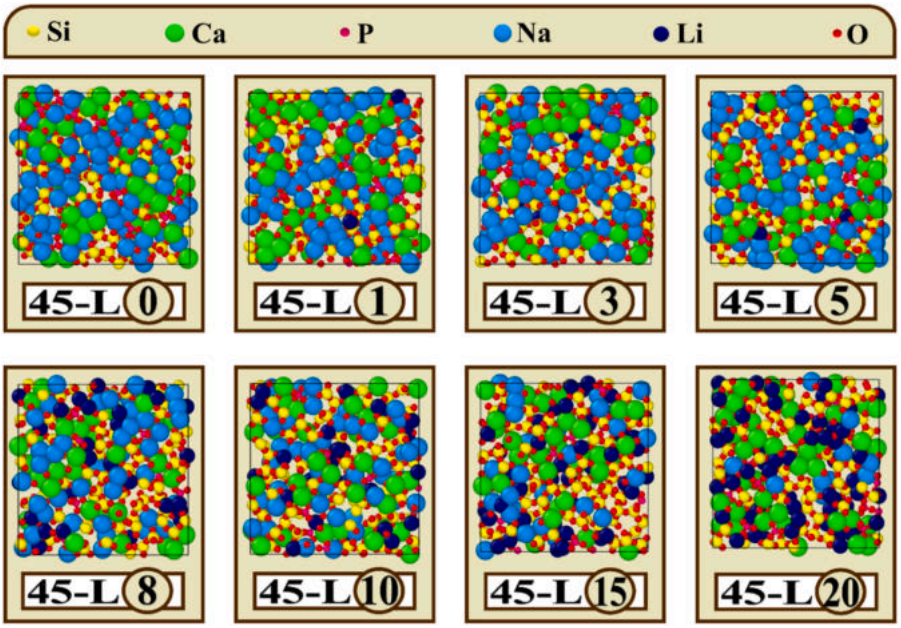


Fig. 1. Simulated structure of the BGs with different Li_2O content, each sphere representing one single atom (yellow: Si, green: Ca, pink: P, light blue: Na, dark blue: Li, red: O).

2.3. Statistical analysis

For each glass composition, three independent MD simulations were performed, and three independent ICP-AES measurement where carried out. Additionally, the results are presented as mean ± standard deviation, and relative error bars have been presented in the corresponding figures.

3. Results and discussion

3.1. Short-range structure

Before examining the intermediate-range structure of the BGs simulated in this study, the short-range structure is first studied using characteristics such as PDF and CN. After obtaining the bond distribution function, the average X-O CN is calculated based on the distance from X (X: Si, P, Ca, Na, Li) using Eq. (2). The obtained results for PDF are shown in Fig. 2. The average lengths of Si–O and P–O bonds were 1.606 ± 0.054 Å and 1.490 ± 0.042 Å, respectively. Furthermore, concerning the bonds of the network modifying elements with oxygen, the bond lengths were 2.369 ± 0.0097 Å, 2.370 ± 0.0190 Å, and 1.949 ± 0.090 Å for Ca–O, Na–O, and Li–O, respectively.

These results show that the lengths of Si–O and P–O bonds, which are related to network-forming elements, are shorter than the lengths of the network-modifying elements with oxygen. Concerning the Li cation, it was observed that Li-O bond has a shorter length than other cations in the structure, which can be attributed to its small atomic radius: this causes Li to occupy less space than Na and, as a result, the molar volume of BGs decreases. In an MD study, Tilocca et al. [41] reported the Si–O bond length to be approximately 1.6 Å, which is in excellent agreement with the findings of the present work. In another study by Gong et al. [42], the Ca–O bond length was reported to be 2.36 Å. Al-Hasni et al. [43] reported the P–O bond to be between 1.49 Å and 1.59 Å, which is consistent with the results reported in this study. Other estimations of modifier–oxygen bond lengths were given by Huang et al. [44] (Na–O bond length equal to 2.4 Å) and Asahi et al. [45] (Li–O bond length equal to 1.9 Å).

$$CN_{ij} = 4\pi\rho_j \int_0^r g_{ij}(r) r^2 dr \quad (2)$$

The average CN of X–O bonds was calculated (Fig. 3) according to their first coordination shell which is determined based on Cutoff radius mentioned in Table 3. The average CN of Si-O and P-O was calculated to be 4.0 ± 0.0002 and 4.0 ± 0.0, respectively, which indicates that the short-range structures of the glass network are SiO_4 and PO_4. The average CN of Ca-O and Na-O was obtained to be 6.277 ± 0.049 and 6.590 ± 0.089, respectively, when the cut-off radius was 3.1 Å and 3.3 Å, respectively. These results showed that Ca and Na form a

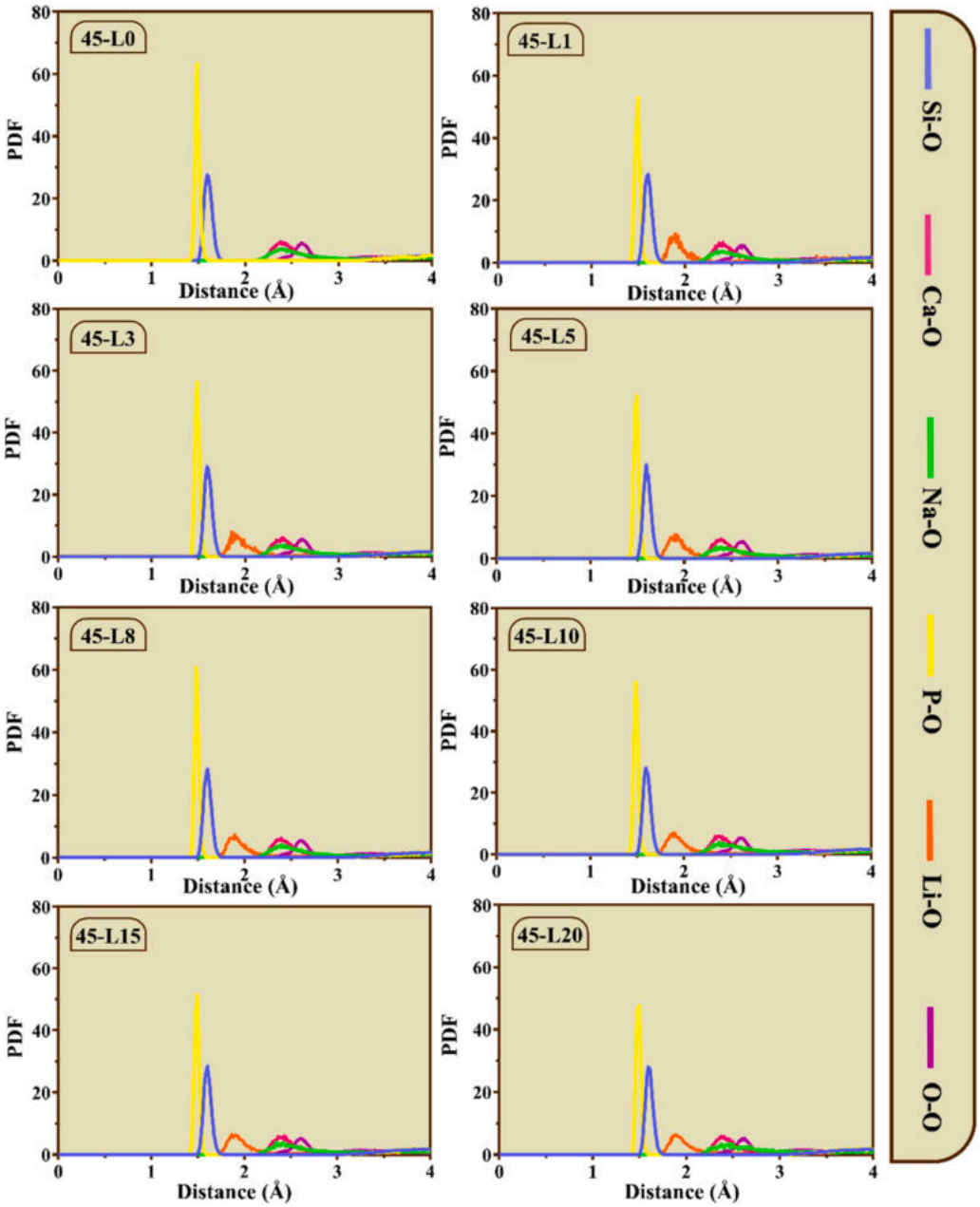


Fig. 2. Pair distribution function of bonds in L-BGs.

structure close to the octahedral one with their surrounding oxygens. The average CN of Li-O was also calculated to be 3.470 ± 0.044. However, the results show that with the increase of Li_2O amount in the composition of the simulated BGs, the average CN of Li-O, Ca-O, and Na-O also increases. The increase in the average CN of these bonds can be attributed to the average Li-O CN because it is lower than the CN of Na-O, and the difference is about 2. As a result, by replacing one Li atom with Na, almost two oxygens attached to Na can no longer be attached to Li, and these two oxygens must bond with other cations or Li itself, which increases the number of O bonds with the cations of the network and also increases the average CN while increasing Li_2O. According to the study of Malavasi et al. [46], the Si-O CN was obtained to be 4 in a wide range of glasses, which indicates that the network building unit of silicate glasses is tetrahedral. The results reported by Mead et al. [47] reported the Ca-O CN in the range of 5.4–6.4. According to the study of Xiang et al. [48], the average Na-O CN was obtained in the range of 5.6–5.8. In another study by Du et al. [49], the average P-O CN was reported to be 4.0 According to the study by Zekri et al. [50], the average Na–O CN was reported to be in the range of 5.46–5.95. The difference between those values and the results obtained in the present study can be attributed to the different chemical compositions of the simulated glass systems. Similarly, in another study [51], an average Li–O bond length of 2.01 Å and an average Li–O CN of 3.7 were reported, which are also in good agreement with the findings of this study.

3.2. *Distribution and density of bonds*

In order to investigate the network continuity, the distribution of the type of oxygen in the structure was investigated. In this study, O with at least one network modifier atom is called a non-bridging oxygen (NBO), and the bridging oxygens (BOs) are classified into three categories: Si-O-Si, Si-O-P, and P-O-P. The obtained results are shown in Fig. 4 and Table 4. According to these results, it is observed that the distribution of P-O-P and Si-O-P is approximately 0% and 2%, respectively.

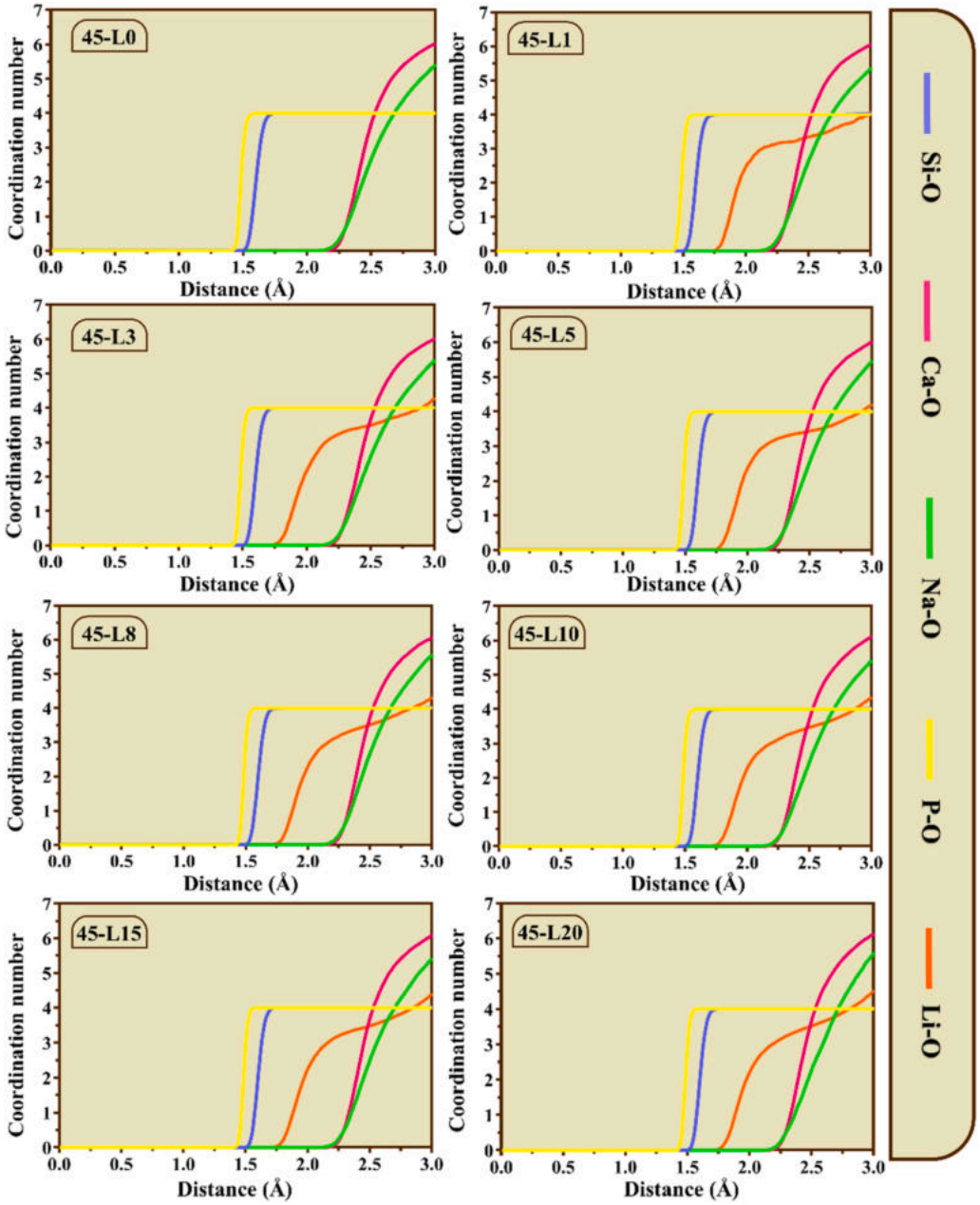


Fig. 3. Coordination number of atoms in L-BGs.

Table 3
PDF first peak and minima, cutoff distance, and average coordination number of X-Os.

X–O bonds	First Peak	First minima	Cutoff distance	Average CN
Si–O	1.596 ± 0.0043	1.80 ± 0.01	2.0	4.0 ± 0.0002
Ca–O	2.369 ± 0.0097	3.141 ± 0.065	3.1	6.277 ± 0.049
Na–O	2.37 ± 0.019	3.315 ± 0.425	3.3	6.590 ± 0.089
P–O	1.490 ± 0.005	1.605 ± 0.010	2.0	4.0 ± 0.0
Li–O	1.95 ± 0.0057	2.403 ± 0.068	2.5	3.470 ± 0.044

Furthermore, the distribution of NBOs is, on average, 68%. The type of oxygen does not change with the substitution of Li_2O instead of Na_2O. Therefore, it can be expected that the substitution of Li_2O does not change the distribution of broken bonds in the network. It is also observed that the distribution of Si–O–Si bonds is about 30%, which is higher compared to other bonds: this is due to the dominance of the silicate network distribution over the phosphate network, which is due to the higher amount of SiO_2 than P_2O_5. As mentioned, due to the dominance of the silicate network over the phosphate network, there is almost no P-O-P bond in the network of BGs. The density of oxygen was also investigated, as shown in Fig. 4**a**. It is observed that with increasing the amount of Li_2O in BGs, the density of Si-O-Si, total oxygens, and NBOs increases. This increase for Si-O-Si, NBOs and total oxygens is from 12 (Bonds/nm^3) to 13.4 (Bonds/nm^3), from 28.00 (Bonds/nm^3) to 30.05 (Bonds/nm^3), and from 40.91 (Bonds/nm^3) to 44.33 (Bonds/nm^3), respectively. Since the distribution of oxygen types and the number of oxygen is constant, reducing the volume of the simulation box increases the density of the aforementioned items. Therefore, it is expected that

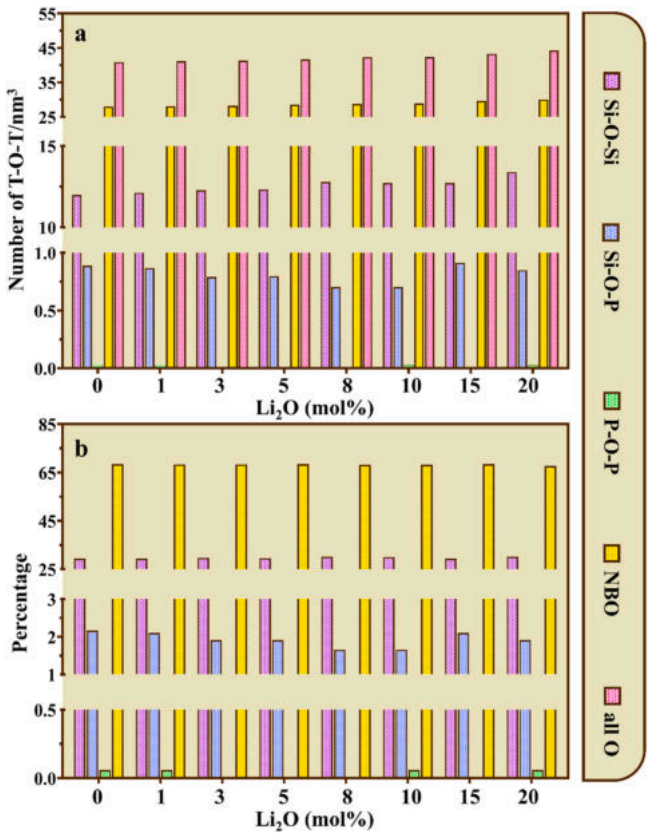


Fig. 4. (a) Oxygen bond density, (b) Oxygen bond type distribution.

there will be more oxygen at the contact surface between the Li_2O-rich BGs and the biological solution. Hence, for the same thickness of the BGs simulated in this study, the Li_2O-rich BGs degrade more slowly. Since the distribution of P-O-P and Si-O-P is generally low in the structure and no significant changes in their density have been observed, these bonds are generally less important in simulated BGs and do not play a role in determining the balanced composition.

3.3. Q^n distributions, network connectivity, and F_{net}

To examine the network connections in detail, the distribution of Q^n was first examined. Q^n are species of network-forming unit structures, such as SiO_4 and PO_4, where n is the number of BOs. A detailed examination of the distribution of Q^n species is important in determining some key properties of BGs, like the solubility. Using the distribution of Q^n, the number of network connections can be obtained according to Eq. (3) [52]. Figs. 5**a** and 5**b** show the distribution of Q^n and the NC of the simulated BGs, respectively. Moreover, the distribution values of Q^n and NC are reported in Table 5. The results show that the distribution of Q^0 for the simulated BGs is approximately equal to 8.41% ± 0.80%. The distribution of Q^1, Q^2, Q^3, and Q^4 is also equal to 24.76% ± 1.48%, 36.72% ± 1.95%, 25.19% 25.20 ± 0.99%, and 4.92% 4.91 ± 0.50% on average, respectively. These results indicate that the highest distribution of Q^n is related to Q^2, which is one of the important characteristics of 45S5 BGs that have a chain structure. The NC for the simulated BGs is approximately 1.935 ± 0.014, but this value has also increased with increasing Li_2O. The results of the distribution of Q^2 and Q^3 show that, with increasing Li_2O and decreasing Na_2O, the distribution of Q^2 has a decreasing trend while the distribution of Q^3 has also increased; on the contrary, the value of other Q^n is approximately constant, and the changes are small compared to these types of Q^n. This trend has increased the density of the structure and, as a result, the NC has increased in general with higher Li_2O content, while increasing Q^3 and decreasing Q^2. However, structural fluctuations of the amorphous BG and the limitations of the MD simulation cause the NC not to have a monotonic behavior, yet the results follow a general increase in NC. Taken together, it can be suggested that, by replacing Li_2O with Na_2O, the degradability of BGs can potentially decrease. This finding is consistent with previous studies on silicate-based glass systems, where changes in the composition of the glasses and the status of network-modifying elements govern the Q^n distribution and NC [53].

In order to investigate the strength of the simulated BGs, Eq. (4) [54] was used to acquire the measurements of F_{net} as an indicator of the structure strength (Fig. 5**c**). This parameter is used to quantify the structural strength using cation interactions, BOs, and NC, to better evaluate the chemical durability of a certain glass composition and shows how tightly bound the glass structure is. According to this relationship, N is the total number of atoms, X is the cations in the structure, CNx-o is the average CN of the X–O bond, and SBS is the single-bond strength; the estimates for these values were taken from Sun's research [55]. According to the obtained results, it can be seen that the network strength trend increases with increasing Li_2O and decreasing Na_2O. These results, together with those about the distribution of Q^2, Q^3, NC, and the density of X-Os, indicate that by replacing Li_2O with Na_2O, the degradability of BGs decreases, and therefore they are expected to exhibit less ion release in biological fluids or solutions.

$$NC = \sum_{n=1}^{4} Q^n.n \tag{3}$$

$$F_{net} = \frac{1}{N}\sum_{X}^{Cation} n_X CN_{X-O} SBS_{X-O} NC \tag{4}$$

3.4. Ion clustering

The homogeneity of BGs is important because the more heterogeneous the BGs are, the more uneven the ion release and the more the structure of the BGs will be, which will reduce the efficiency of BGs in therapeutic applications. The homogeneity of BGs can also contribute to sudden changes in NC. In addition, clustering can increase the tendency of crystalline phases to develop from the patent glass, which may affect bioactivity. Eq. (5) [52] allows calculating the R factor, which is used to calculate the degree of structural homogeneity and the tendency of

Table 4
Ratio and density of oxygen bonds in the L-BGs.

BGs	Ratio of Bonds (%)				Density of Bonds (Bonds/nm³)				
	Si-O-Si	Si-O-P	P-O-P	Non BO	Si-O-Si	Si-O-P	P-O-P	Non BO	All X-O
45-L0	29.33%	2.17%	0.06%	68.43%	11.99865	0.888789	0.026141	27.99685	40.91043
45-L1	29.46%	2.11%	0.06%	68.37%	12.12219	0.867749	0.026295	28.1361	41.15233
45-L3	29.71%	1.92%	0.00%	68.37%	12.27239	0.791767	0	28.2397	41.30386
45-L5	29.58%	1.92%	0.00%	68.50%	12.33509	0.79925	0	28.55986	41.69419
45-L8	30.22%	1.66%	0.00%	68.12%	12.79029	0.70306	0	28.82547	42.31882
45-L10	30.03%	1.66%	0.06%	68.24%	12.73343	0.704402	0.027092	28.93468	42.3996
45-L15	29.39%	2.11%	0.00%	68.50%	12.72506	0.912885	0	29.65492	43.29287
45-L20	30.22%	1.92%	0.06%	67.80%	13.39802	0.849769	0.028326	30.05348	44.32959

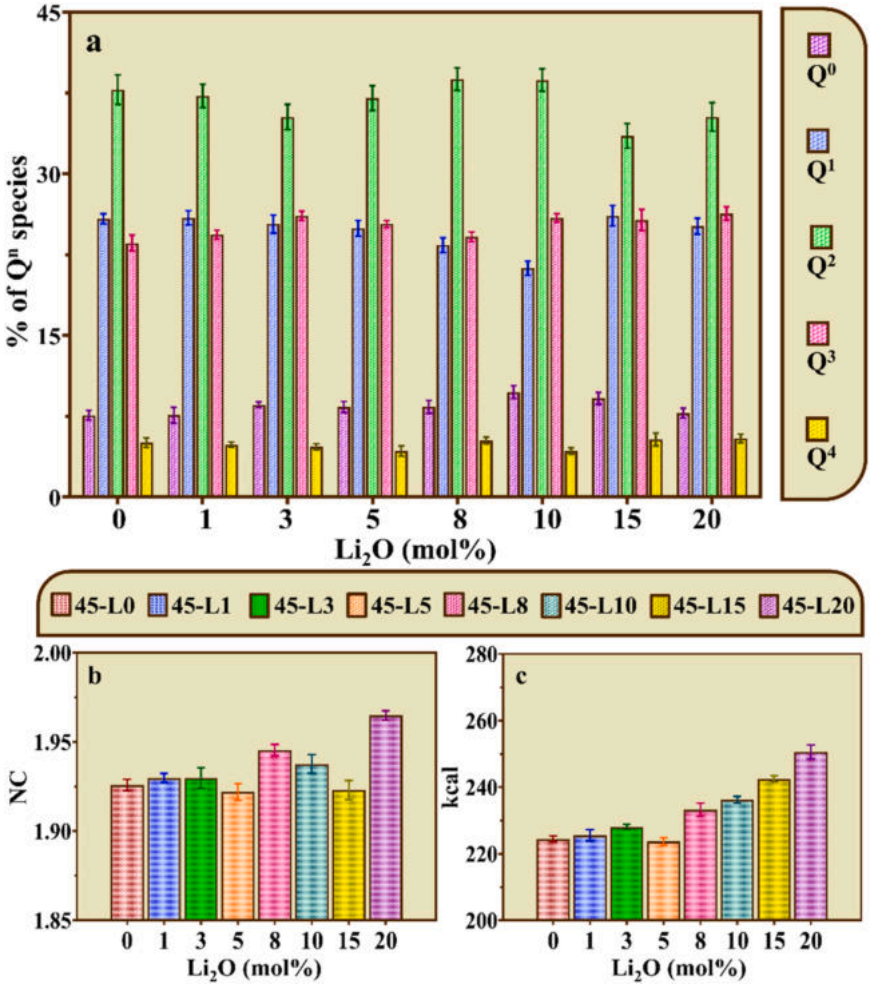


Fig. 5. Medium-range structural properties of L-BGs are shown as (a) Q^n distribution, (b) Network connectivity (NC), (c) F_{net}.

Table 5
Q^n distribution and network connectivity of L-BGs.

BGs	NC	Q^0 (%)	Q^1 (%)	Q^2 (%)	Q^3 (%)	Q^4 (%)
45-L0	1.9259 ± 0.0031	7.60 ± 0.45	25.84 ± 0.46	37.82 ± 1.37	23.59 ± 0.74	5.07 ± 0.44
45-L1	1.9298 ± 0.0025	7.61 ± 0.73	25.93 ± 0.65	37.23 ± 1.08	24.37 ± 0.42	4.87 ± 0.24
45-L3	1.9298 ± 0.0058	8.58 ± 0.27	25.34 ± 0.84	35.28 ± 1.18	26.12 ± 0.43	4.68 ± 0.28
45-L5	1.9220 ± 0.0047	8.37 ± 0.52	24.95 ± 0.73	37.04 ± 1.16	25.34 ± 0.34	4.29 ± 0.48
45-L8	1.9454 ± 0.0032	8.38 ± 0.60	23.39 ± 0.67	38.79 ± 1.06	24.17 ± 0.44	5.26 ± 0.32
45-L10	1.9376 ± 0.0052	9.75 ± 0.60	21.25 ± 0.66	38.71 ± 1.04	25.93 ± 0.38	4.29 ± 0.29
45-L15	1.9230 ± 0.0054	9.16 ± 0.56	26.12 ± 0.95	33.53 ± 1.15	25.73 ± 0.98	5.36 ± 0.59
45-L20	1.9649 ± 0.0026	7.80 ± 0.46	25.15 ± 0.74	35.28 ± 1.32	26.32 ± 0.63	5.46 ± 0.40

atoms to be clustered with each other, to measure the homogeneity of BGs. Fig. 6 and Table 6 show the R factor for the homogeneous distribution of cations in the chemical composition. As long as R is greater than 1, the X atoms form clusters in the structure, while if R = 1, the distribution is uniform.

The results show that the distribution of Ca in the structure of the simulated BGs is constant and does not change with increasing Li_2O and decreasing Na_2O, but the distribution of Na and Li in the simulated BGs is inversely proportional to each other. In this way, the distribution of Na in Na-rich compounds is almost constant, but with increasing Li_2O in the BG, the distribution of Na becomes more heterogeneous. The reason for this can be attributed to the lower number of Na atoms in the simulation box, which causes the Na atoms to be located in very close or very far positions relative to each other, while in high amounts of Na atoms these atoms fill the empty positions in the structure that were in the low number state; as a result, the distance between Na atoms tends to constant values, which causes the distribution of Na atoms to be homogeneous. In the simulation data, Na atoms in the 45-L20 BG did not fill a series of sites on the surface, but in the 45-L0 BG, almost the entire surface was filled with Na atoms. These cases also apply to Li homogeneity, and hence it can be seen that in BGs poor in Li_2O, the $R_{Na\text{-}Na}$ factor tends to 1, but the $R_{Li\text{-}Li}$ factor shows values higher than 3.0, which indicates the heterogeneous distribution of Li atoms in these compounds. On the contrary, in compounds rich in Li_2O, the $R_{Li\text{-}Li}$ factor tends to 1, and the $R_{Na\text{-}Na}$ factor reaches values higher than 2.0. Promising values of the $R_{Li\text{-}Li}$ and $R_{Na\text{-}Na}$ factors are observed in the BGs 45-L5, 45-L8, and 45-L10. The values of $R_{Na\text{-}Na}$ and $R_{Li\text{-}Li}$ in 45-L10 glass are close to each other compared to other BGs, which indicates that the distribution of these atoms in the structure is similar to each other.

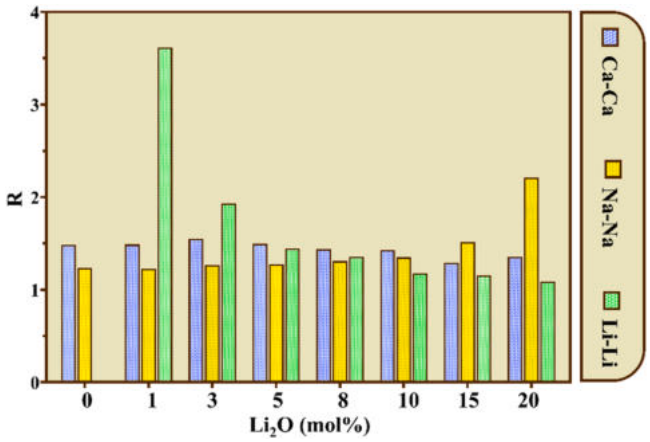


Fig. 6. Ion clustering analysis of L-BGs as an indication of the tendency of atoms to be clustered to each other.

$$R_{X-X} = \frac{CN_{X-X} + 1}{4/3 \times \pi r^3 \times \left(\frac{N_X}{V}\right)} \quad (5)$$

3.5. Experimental Evaluation

3.5.1. Ion release

Fig. 7**a** shows the release rate of Si ions from the surface of BG samples doped with Li_2O in SBF during 24 h of immersion. According to the results, the dependence of the release behavior of Si ions from the glass surface on time was confirmed in all samples, and with increasing Li_2O content in the chemical composition of the samples, the concentration of Si ions measured in SBF decreased. The highest release rate of Si ions was reported for L0–45, and the concentration of Si ions released in SBF decreased monotonically with higher Li_2O content. Moreover, the results were in accordance with the network structure of the glass samples predicted by MD simulations, and the decrease in Si ion release in samples containing higher amounts of Li_2O was confirmed by increasing Si-O-Si bonds and the amount of NC in the simulated glass network. In addition, according to Fig. 7**b**, the different behavior of Li ion release from the surface of the samples was shown compared to Si release: the rate of Li ion release from the surface of the BG samples in SBF increased with increasing immersion time and the amount of Li_2O in the chemical composition of the samples. Furthermore, the release rate of Li ions from the surface of the samples increased with a greater slope up to 6 h after immersion of the samples in SBF due to the dissolution of the glass network and after that, the highest and lowest release rates were observed in samples 45-L20 and 45-L1, respectively, up to 24 h of immersion. The amount of Li ions released from sample 45-L0 was

Table 6
Ion clustering data of BGs.

BGs	45-L0	45-L1	45-L3	45-L5	45-L8	45-L10	45-L15	45-L20
R_{Ca-Ca}	1.486418	1.489436	1.548976	1.496766	1.439235	1.429647	1.291199	1.357037
R_{Li-Li}	-	3.618937	1.933863	1.443801	1.355663	1.178661	1.156669	1.08914
R_{Na-Na}	1.236846	1.225514	1.267403	1.275872	1.310798	1.351868	1.514168	2.211373

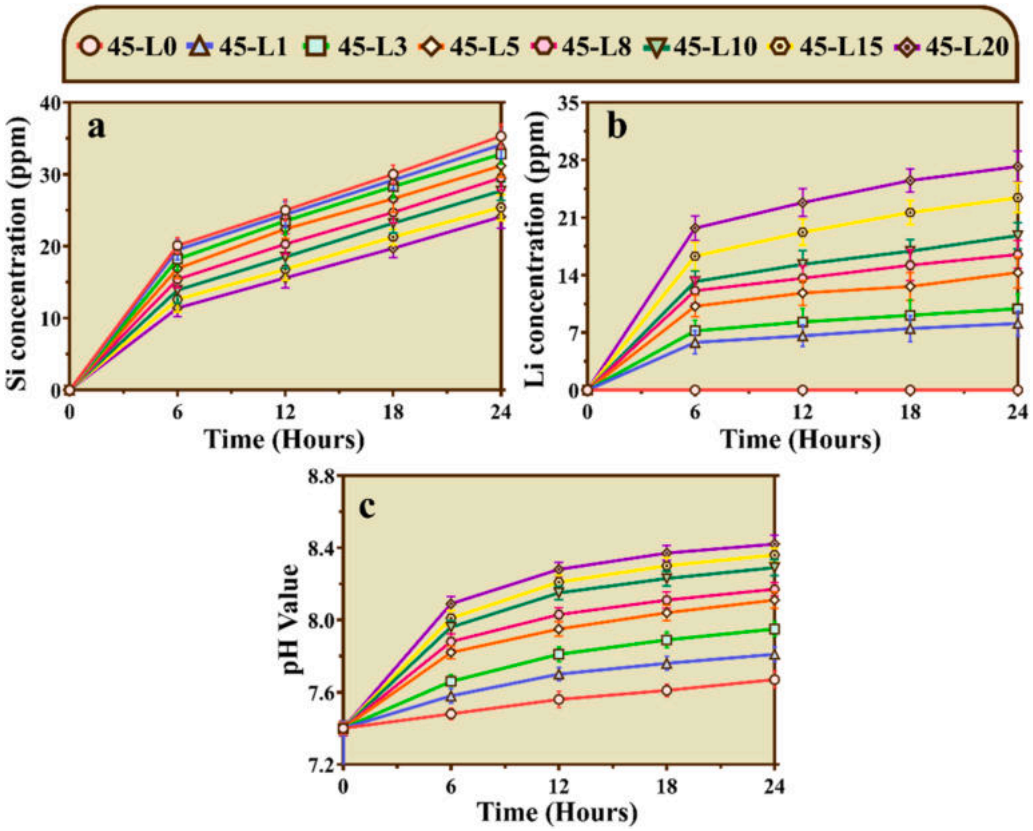


Fig. 7. ICP-AES evaluation of SBF after 24 h of BGs immersion, presenting Si and Li concentrations and pH values.

measured to be zero up to 24 h of immersion in the SBF solution due to the absence of Li_2O in its chemical composition. In addition, in order to accurately investigate the ion exchange and dissolution of the BG network, the pH of the SBF of the studied samples was measured, and the results are presented in Fig. 7**c**. According to this figure, the presence of Li_2O in the chemical composition of the samples, due to its alkaline property, led to an increase in the pH of the SBF. Meanwhile, the pH of the SBF of the samples increased at a high rate during the first 6 h of immersion due to the dissolution of the glass network and the rapid exchange of alkali ions Na^+ and Li^+ with H_3O^+ from the solution. In addition, according to the results of glass simulation, with the increase in Li_2O in the chemical composition of the samples, the NBO content also increased, which is in accordance with the increase in the number of sites available for ion exchange due to the location of the alkali ion modifiers Li^+ in the BG network. The combined MD and experimental results indicate that the investigated compositions exhibit a trade-off between structural stability and dissolution behavior. Higher Li_2O content leads to enhanced NC, Q^3 fraction, oxygen density, and F_{net}, resulting in a more polymerized glass network and reduced Si ion release. Additionally, lower Li_2O contents showcased high Li-ion aggregation, which may lead to non-uniform ion distribution. In contrast, BGs with higher Li_2O content exhibited improved structural homogeneity but lower dissolution, due to the lower network polymerization. Taken together, among the investigated compositions, 45-L5 provides a promising combination of structural stability, homogeneous Li distribution, and controlled ion release.

3.5.2. *In vitro bioactivity*

Fig. 8 displays SEM images of the 45-L5 sample after 14 days of immersion in SBF. As observed, the surface is almost completely covered by a newly-formed layer with globular agglomerates on the top. This cauliflower-like morphology is the typical "fingerprint" of the apatite-like Ca-P layers that were commonly reported to cover the surface of BGs after immersion in SBF. Although this morphology is fully consistent with apatite formation on various types of silicate BGs [56,57] – and can thus further support the ionic dissolution of the 45-L5 yielding such a new phase –, SEM alone cannot conclusively identify the nature of this phase as crystalline HA, which would need to be confirmed by complementary investigations like XRD. Microcracks are usually observed in this newly-formed layer due to the prolonged immersion and the volume change of the sample after drying [58]. Higher magnifications showed spheres with cauliflower-like morphology with sub-micron sizes. The packed morphology of the spheres has sustained the nucleation and growth process, while being supported by the moderate ion release process of the 45-L5 sample in SBF. This Ca-P layer development after 14 days of immersion confirms the *in vitro* bioactivity of the 45-L5 sample and its potential for bone TE applications.

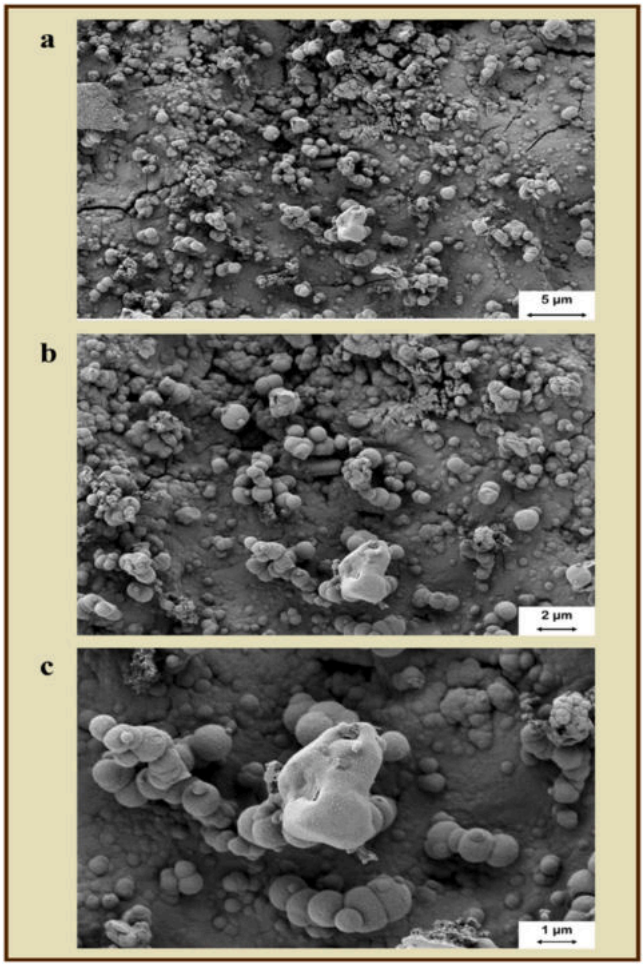


Fig. 8. SEM micrographs of the 45-L5 sample after 14 days of immersion in SBF with magnifications of (a) 3 k×, (b) 5 k×, and (c) 10 k×.

4. Conclusions

This study utilized LAMMPS software to simulate Li-doped 45S5 BGs (0–20 mol% Li_2O) based on MD simulations. 45-L0 to 45-L20 BGs were synthesized using the melt-quench method, and the Li_2O was substituted with Na_2O to ensure consistency in the charge distribution of the final structure of the simulated L-BGs. To evaluate the structural properties, short- and medium-range structures were analyzed as in properties of PDF, CN, oxygen bonds, Q^n species, NC, F_{net}, and ion clustering. Additionally, ICP-AES and SEM were used to ensure the experimental evaluations were in line with simulation data. PDF curves showed a 1.606 Å length for Si–O bonds and a CN of 4, determining the tetrahedral formation in the glass structure by the silicate network. Moreover, Li-O had the shortest bond length among the modifying atoms of the structure, with 1.949 Å in length. The Q^n distribution favored Q^3 with higher Li_2O content, leading to an increasing NC, hence a more integrated structure in the BGs. Ion clustering showed a homogeneous distribution of atoms for moderate Li_2O contents in BGs; therefore, 45-L5 was considered a promising candidate according to MD results to have controlled and balanced release of ions in the SBF. In addition, ICP-AES analysis showed that the Si ion release rate was reduced with higher Li_2O content during the 24 h SBF immersion, and pH values of the SBF were increased; meanwhile, the SEM images of 45-L5 revealed the formation of an apatite-like Ca-P surface layer on the surface of the sample after 14 days of immersion in SBF, indicating sustained ion release and bioactivity. Taken together, the dissolution of the BGs in the physiological environment leads to a beneficial role in designing valuable biomaterials for TE applications. Overall, based on the MD simulations data and experimental evaluations, 5 mol% of Li_2O substitution for Na_2O in the composition of 45S5 bioglass was expected to have favorable results of degradability and bioactivity, therefore making this glass a promising candidate to be used in TE and biomedical applications.

CRediT authorship contribution statement

Moghanian Amir: Writing – original draft, Methodology, Investigation, Formal analysis, Data curation, Conceptualization. **Francesco Baino:** Writing – review & editing, Validation, Methodology.

Declaration of Competing Interest

The authors declare that they have no known financial or personal conflict of interest related to this manuscript.

Acknowledgements

This article received no funding.

Data availability statement

Data will be made available to Readers on request.

References

[1] L.L. Hench, The story of bioglass®, J. Mater. Sci.: Mater. Med. 17 (11) (2006) 967–978.
[2] F.F. Bakare, B.G. Ewente, T.C. Akililu, A.D. Jara, G.M. Gonfa, Synthesis and characterization of bioactive glass via CTAB modified sol-gel method for in vitro biological activities, J. Biomed. Mater. Res. Part B: Appl. Biomater. 113 (3) (2025) e35548.
[3] H. Madival, A. Rajiv, A comprehensive review of bioactive glasses: synthesis, characterization, and applications in regenerative medicine, Biomed. Mater. Devices (2025) 1–21.
[4] A. Moghanian, H.J. Haugen, D. Marović, From atomic scale to biological performance: the role of magnesium in solubility of the network and bioactivity of 45S5 Bioglass®, J. Non-Cryst. Solids 680 (2026) 124046.
[5] S.S. Shendage, G. Kamble, R. Chavan, N.R. Jadav, R.-a. Doong, J.-Y. Chang, A. V. Ghule, Bioactive glass for bone tissue regeneration: focusing on the key biological properties, ACS Biomater. Sci. Eng. (2025).
[6] A. Moghanian, F. Baino, Machine learning–assisted structural characterization of ring size distribution in Sr-doped bioactive glasses: a molecular dynamics study, Ceram. Int. (2026).
[7] B.A. Ben-Arfa, R.C. Pullar, A comparison of bioactive glass scaffolds fabricated by robocasting from powders made by sol–gel and melt-quenching methods, Processes 8 (5) (2020) 615.
[8] A. Moghanian, S. Safaee, A.A. Kızılkurtlu, R. Farmani, Advanced rare-earth doped bioactive glasses: a comprehensive review on structural, biological, and mechanical improvements, Silicon (2025) 1–28.
[9] A. Moghanian, A. Tayebi, R. Farmani, Atomic-to-biological evaluation of rare earth substituted cerium-doped bioactive glasses for biomedical applications using molecular dynamics simulations, J. Rare Earths (2026).
[10] A. Moghanian, S. Safaee, A.A. Kizilkurtlu, R. Farmani, Advanced rare-earth doped bioactive glasses: a review on bioactivity and therapeutic potential, Mater. Today Commun. (2026) 115348.
[11] W. Gao, J. Kang, D. Zhao, J. Si, X. Wu, Y. Yue, Y. Qu, Z. Xiao, N. Zhang, A novel high Q × f value glass-ceramic with ultra-low sintering temperature for ULTCC substrate application, Ceram. Int. (2025).
[12] J. Turner, A. Nandakumar, N. Anilbhai, A.R. Boccaccini, J.R. Jones, G. Jell, The effect of Si species released from bioactive glasses on cell behaviour: a quantitative review, Acta Biomater. 170 (2023) 39–52.
[13] T. Mehrabi, A.S. Mesgar, Z. Mohammadi, Bioactive glasses: a promising therapeutic ion release strategy for enhancing wound healing, ACS Biomater. Sci. Eng. 6 (10) (2020) 5399–5430.
[14] Y. Zhu, X. Zhang, G. Chang, S. Deng, H.F. Chan, Bioactive glass in tissue regeneration: unveiling recent advances in regenerative strategies and applications, Adv. Mater. 37 (2) (2025) 2312964.
[15] A. Hoppe, A.R. Boccaccini, Biological impact of bioactive glasses and their dissolution products, Front. Oral Biol. 17 (2015) 22–32.
[16] H. Sakai, J.I. Sasaki, H. Kitagawa, G.L. Abe, T. Kohno, N. Funayama, S. Imazato, Fabrication of lithium/strontium-releasing smart bioactive glasses with anti-inflammatory and osteogenic effects tailored to pathological stages, Macromol. Biosci. (2025) e00268.
[17] X. Zhang, K. Nan, Y. Zhang, K. Song, Z. Geng, D. Shang, L. Fan, Lithium and cobalt co-doped mesoporous bioactive glass nanoparticles promote osteogenesis and angiogenesis in bone regeneration, Front. Bioeng. Biotechnol. 11 (2024) 1288393.
[18] F.G. Gramajo, M.A. Rivoira, V. Rodríguez, G. Vargas, R.V. Mesones, M.P. Zago, A. R. Boccaccini, A. Gorustovich, Lithium-containing 45S5 Bioglass-derived glass-ceramics have antioxidant activity and induce new bone formation in a rat preclinical model of type 1 diabetes mellitus, Biomed. Mater. 20 (1) (2024) 015006.
[19] A. Moghanian, Atomic structure, network properties, and ring topology of lithium-doped 45S5 bioactive glass: insights from molecular dynamics and machine learning, Ceram. Int. (2026).
[20] H.O. Simila, A.R. Boccaccini, Sol-gel synthesis of lithium doped mesoporous bioactive glass nanoparticles and tricalcium silicate for restorative dentistry: comparative investigation of physico-chemical structure, antibacterial susceptibility and biocompatibility, Front. Bioeng. Biotechnol. 11 (2023) 1065597.
[21] R. Wei, Z. Zhang, M. Xing, Y. Zhou, J. Chang, Preparation and in vitro evaluation of Lithium-doped bioactive glasses for wound healing with nerve repair potential, Mater. Lett. 292 (2021) 129629.
[22] H.P. Cordero, R.C. Cid, M.D. Dosque, R.C. Ibacache, P.P. Fluxá, Li-doped bioglass® 45S5 for potential treatment of prevalent oral diseases, J. Dent. 105 (2021) 103575.
[23] P. Keikhosravani, H. Maleki-Ghaleh, A. Kahaie Khosrowshahi, M. Bodaghi, Z. Dargahi, M. Kavanlouei, P. Khademi-Azandehi, A. Fallah, Y. Beygi-Khosrowshahi, M.H. Siadati, Bioactivity and antibacterial behaviors of nanostructured lithium-doped hydroxyapatite for bone scaffold application, Int. J. Mol. Sci. 22 (17) (2021) 9214.
[24] P.E. Florian, L. Duta, V. Grumezescu, G. Popescu-Pelin, A.C. Popescu, F.N. Oktar, R. W. Evans, A. Roseanu Constantinescu, Lithium-doped biological-derived hydroxyapatite coatings sustain in vitro differentiation of human primary mesenchymal stem cells to osteoblasts, Coatings 9 (12) (2019) 781.
[25] Y. Wang, X. Yang, Z. Gu, H. Qin, L. Li, J. Liu, X. Yu, In vitro study on the degradation of lithium-doped hydroxyapatite for bone tissue engineering scaffold, Mater. Sci. Eng.: C 66 (2016) 185–192.
[26] A. Moghanian, Biocompatibility and dissolution experiments with molecular dynamics structural characterization of melt-derived Mg-substituted silicate bioactive potential glasses, J. Non-Cryst. Solids 672 (2026) 123855.
[27] A. Moghanian, H.J. Haugen, D. Marović, S. Safaee, Role of strontium incorporation on the structural network of 45S5 bioactive glass: a molecular dynamics investigation, Mater. Today Commun. (2026) 115131.
[28] A. Moghanian, A. Pazhouheshgar, A. Rajabpour, Correlating between atomic structure and mechanical properties in cobalt-doped silicate glasses via molecular dynamics and machine learning, Results Eng. (2026) 110575.
[29] A. Moghanian, R. Farmani, A. Tayebi, N. Kolivand, S. Safaee, Investigating zinc-doped silicate-based trinary glass using computational chemistry: a study on interatomic interaction, dissolution behavior, and antibacterial efficiency, J. Non-Cryst. Solids 669 (2025) 123804.
[30] A. Moghanian, M.N. Esfahani, A. Pazhouheshgar, S. Safaee, Molecular dynamics and machine learning insights into Cu-doped silicate-based bioactive glasses: from radial distribution function to ring size distribution, Mater. Today Commun. (2026) 114909.
[31] A. Moghanian, A.A. Kızılkurtlu, S. Safaee, F. Baino, A. Akpek, M. Vaseghi, Molecular dynamics simulations in biomaterials science: atomistic modeling across bioactive glasses and ceramics, polymers, metals and composites, Mater. Today Commun. (2026) 115306.
[32] A. Moghanian, 3D convolutional neural network–driven ring size distribution prediction in magnesium-doped 45S5 bioactive glasses: an integrated molecular dynamics–machine learning framework, Mater. Res. Bull. (2026) 114222.
[33] J. Du, Y. Xiang, Effect of strontium substitution on the structure, ionic diffusion and dynamic properties of 45S5 bioactive glasses, J. Non-Cryst. Solids 358 (8) (2012) 1059–1071.
[34] L. Deng, J. Du, Development of boron oxide potentials for computer simulations of multicomponent oxide glasses, J. Am. Ceram. Soc. 102 (5) (2019) 2482–2505.
[35] A. Moghanian, Computational insight into the effect of SrO substitution for CaO on the structural properties of simulated silicate-based bioactive glass, Results Mater. (2026) 100980.
[36] S.H. Hosseini, K. Sinkó, I. Varga, A. Moghanian, Molecular dynamic simulation and experimental insights on structure-property relationships in antibacterial Cu-doped silicate-based bioactive glasses, J. Non-Cryst. Solids 683 (2026) 124108.
[37] B.A. Wells, A.L. Chaffee, Ewald summation for molecular simulations, J. Chem. Theory Comput. 11 (8) (2015) 3684–3695.
[38] S. Nosé, A unified formulation of the constant temperature molecular dynamics methods, J. Chem. Phys. 81 (1) (1984) 511–519.
[39] S. Nose, Molecular dynamics simulations, Prog. Theor. Phys.= 理論物理学の進歩/ Yukawa Inst. Theor. Phys. Phys. Soc. Jpn., no. suppl 103, 1991, pp. 1–117.
[40] W.G. Hoover, Canonical dynamics: equilibrium phase-space distributions, Phys. Rev. A 31 (3) (1985) 1695.
[41] A. Tilocca, A.N. Cormack, N.H. de Leeuw, The structure of bioactive silicate glasses: new insight from molecular dynamics simulations, Chem. Mater. 19 (1) (2007) 95–103.
[42] K. Gong, E.A. Olivetti, Development of structural descriptors to predict dissolution rate of volcanic glasses: molecular dynamic simulations, J. Am. Ceram. Soc. 105 (4) (2022) 2575–2594.
[43] B.M. Al-Hasni, G. Mountjoy, E. Barney, Atomic structure of sodium iron phosphate glasses, Int. J. Appl. Glass Sci. 12 (2) (2021) 245–258.
[44] C. Huang, A. Cormack, The structure of sodium silicate glass, J. Chem. Phys. 93 (11) (1990) 8180–8186.
[45] R. Asahi, C.M. Freeman, P. Saxe, E. Wimmer, Thermal expansion, diffusion and melting of Li2O using a compact forcefield derived from ab initio molecular dynamics, Model. Simul. Mater. Sci. Eng. 22 (7) (2014) 075009.
[46] G. Malavasi, L. Menabue, M.C. Menziani, A. Pedone, A. Salinas, M. Vallet-Regí, New insights into the bioactivity of SiO2–CaO and SiO2–CaO–P2O5 sol–gel glasses by molecular dynamics simulations, J. Sol-Gel Sci. Technol. 67 (1) (2013) 208–219.
[47] R.N. Mead, G. Mountjoy, A molecular dynamics study of the atomic structure of (CaO) x (SiO2) 1-x glasses, J. Phys. Chem. B 110 (29) (2006) 14273–14278.
[48] Y. Xiang, J. Du, Effect of strontium substitution on the structure of 45S5 bioglasses, Chem. Mater. 23 (11) (2011) 2703–2717.
[49] J. Du, L. Kokou, J.L. Rygel, Y. Chen, C.G. Pantano, R. Woodman, J. Belcher, Structure of cerium phosphate glasses: molecular dynamics simulation, J. Am. Ceram. Soc. 94 (8) (2011) 2393–2401.
[50] M. Zekri, A. Herrmann, C. Rüssel, R. Maâlej, Rare earth doped sodium aluminosilicate glasses: structure-property correlations from molecular dynamics simulations and luminescence measurements, J. Alloy. Compd. 1063 (2026) 187657.
[51] M. Zekri, A. Herrmann, A. Erlebach, K. Damak, C. Rüssel, M. Sierka, R. Maâlej, The structure of Gd3+-doped Li2O and K2O containing aluminosilicate glasses from molecular dynamics simulations, Materials 14 (12) (2021) 3265.
[52] D. Presti, F. Muniz-Miranda, F. Tavanti, A. Pedone, Structure analysis and properties calculations, At. Simul. Glass. Fundam. Appl. (2022) 89–122.

[53] W. Gao, J. Li, Y. Lu, L. Liu, Y. Yue, S. Shen, J. Kang, Preparation and structural control of high-performance, low expansion electronic glass fibers for chip carriers, Ceram. Int. (2026).
[54] A. Atila, Y. Ouldhnini, S. Ouaskit, A. Hasnaoui, Atomistic insights into the mixed-alkali effect in phosphosilicate glasses, Phys. Rev. B 105 (13) (2022) 134101.
[55] K.H. Sun, Fundamental condition of glass formation, J. Am. Ceram. Soc. 30 (9) (1947) 277–281.
[56] A. López-Noriega, D. Arcos, I. Izquierdo-Barba, Y. Sakamoto, O. Terasaki, M. Vallet-Regí, Ordered mesoporous bioactive glasses for bone tissue regeneration, Chem. Mater. 18 (13) (2006) 3137–3144.
[57] E. Fiume, D. Tulyaganov, G. Ubertalli, E. Verné, F. Baino, Dolomite-foamed bioactive silicate scaffolds for bone tissue repair, Materials 13 (3) (2020) 628.
[58] J. Chen, L. Zeng, X. Chen, T. Liao, J. Zheng, Preparation and characterization of bioactive glass tablets and evaluation of bioactivity and cytotoxicity in vitro, Bioact. Mater. 3 (3) (2018) 315–321.